IEEE Photonics Journal
An IEEE Photonics Society Publication

Open Access

Modeling of Edge-Emitting Lasers Based on Tensile Strained Germanium Microstrips

Volume 7, Number 3, June 2015

D. Peschka
M. Thomas
A. Glitzky
R. Nürnberg
K. Gärtner
M. Virgilio
S. Guha
Th. Schroeder
G. Capellini
Th. Koprucki

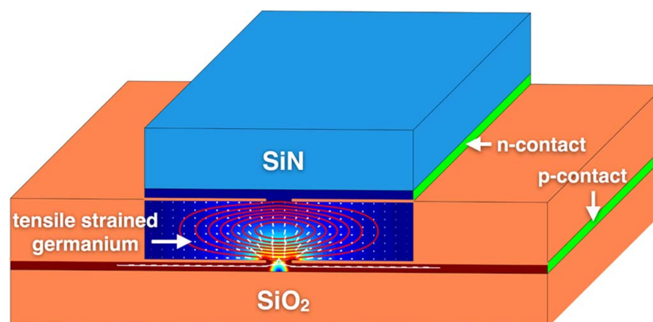

DOI: 10.1109/JPHOT.2015.2427093
1943-0655 © 2015 IEEE

IEEE photonics SOCIETY
IEEE

Modeling of Edge-Emitting Lasers Based on Tensile Strained Germanium Microstrips

D. Peschka,[1] M. Thomas,[1] A. Glitzky,[1] R. Nürnberg,[1] K. Gärtner,[2] M. Virgilio,[3] S. Guha,[4] Th. Schroeder,[4] G. Capellini,[4] and Th. Koprucki[1]

[1]Weierstraß-Institut, 10117 Berlin, Germany
[2]Institute of Computational Science, Universita della Svizzera Italiana, 6904 Lugano, Switzerland
[3]Dipartimento di Fisica "E. Fermi," Università di Pisa, 56127 Pisa, Italy
[4]IHP, 15236 Frankfurt (Oder), Germany

DOI: 10.1109/JPHOT.2015.2427093
This work is licensed under a Creative Commons Attribution 3.0 License. For more information, see http://creativecommons.org/licenses/by/3.0/

Manuscript received February 14, 2015; revised April 20, 2015; accepted April 24, 2015. Date of publication April 29, 2015; date of current version May 19, 2015. The work of D. Peschka and M. Thomas was supported by the MATHEON-Project OT1 "Mathematical modeling, analysis, and optimization of strained germanium-microbridges," within the Einstein Center for Mathematics Berlin. The work of A. Glitzky was supported by the MATHEON-Project SE2 "Electrothermal modeling of large-area OLEDs," within the Einstein Center for Mathematics Berlin. The work of Th. Koprucki was supported by the Deutsche Forschungsgemeinschaft (DFG) within the Collaborative Research Center 787 "Semiconductor Nanophotonics." Corresponding author: Th. Koprucki (e-mail: Thomas.Koprucki@wias-berlin.de).

Abstract: In this paper, we present a thorough modeling of an edge-emitting laser based on strained germanium (Ge) microstrips. The full-band structure of the tensile strained Ge layer enters the calculation of optical properties. Material gain for strained Ge is used in the 2D simulation of the carrier transport and of the optical field within a cross section of the microstrips orthogonal to the optical cavity. We study optoelectronic properties of the device for two different designs. The simulation results are very promising as they show feasible ways toward Ge emitter devices with lower threshold currents and higher efficiency as published insofar.

Index Terms: Semiconductor lasers, semiconductor materials, strain, doping, germanium.

1. Introduction

The realization of monolithically integrated light sources represents today the holy grail of silicon photonics and different approaches have been proposed to fulfill this demand [1], [2]. The pioneering work of MIT researchers has led to the demonstration of both optically [3] and electrically [4] pumped lasers based on a slightly tensile strained germanium (Ge) layer. Unfortunately, the electrically pumped device had a very limited efficiency and it suffered from an extremely high lasing threshold current density of 300 $kAcm^{-2}$, which reduced its operating lifetime to a few minutes. Band engineering of Ge through application of higher tensile strain appears to be a promising way to increase the optical gain [5] and a plethora of different strategies have been proposed. In this way relatively high values of biaxial and uniaxial strain were obtained (see Boucaud *et al.* [6] for a review). Nevertheless, the proposed methods rely either on non CMOS-qualified materials (such as Ge on III-V substrates [7] or Ge on GeSn alloys [8], [9]), or on fabrication schemes leading to microstructures having shapes and/or sizes which prevent their embedding into standard fabrication processes, at least on the short-medium term [10], [11].

We recently proposed an approach based on tensile strained Ge microstrips realized in a CMOS-prototyping line featuring a 130 nm technology [12]. The tensile strain is induced by the elastic relaxation that occurs after the lithographic definition of a microstructure. This microstructure consists of a compressively stressed SiN layer deposited on top of a Ge/Si heterostructure fabricated on top of a silicon-on-insulator substrate (SOI). Uniaxial strain values in excess of 1.5% have been obtained. The Ge microstrips show a spatially homogeneous strain distribution over any investigated length. Furthermore they exhibit an enhancement of the photoluminescence (PL) intensity of more than one order of magnitude with respect to thermally strained Ge/Si layers, such as in the MIT device. The strain relaxation process has been thoroughly investigated with the help of FEM simulation, Raman spectroscopy [12], [13], and advanced micro-diffraction techniques [14].

Recently, we also modeled the optical properties of tensile strained Ge structures using a multi-valley effective mass approach in conjunction with full band structure tight binding calculations [15], [16]. The theoretical predictions were tested against photoluminescence data and a very good agreement was obtained. This allows us to use the optical modeling in a predictive way. After these promising preliminary works, we have conceived a fully integrated laser based on a linear Fabry–Perot cavity formed by tensile strained, highly n-type doped Ge microstrips manufactured by a standard CMOS process [17].

So far, theoretical investigations of threshold currents for Ge lasers are either based on rate equation models which qualitatively describe effects of strain and excitation, e.g., [10], [18], or are based on 1D simulations for the carrier transport using only drift-diffusion models without optical fields [19]–[21]. The latter cannot treat 2D carrier transport effects relevant for the accurate description of the carrier injection into the optical mode. This is of particular importance for realistic device concepts utilizing a spatially inhomogeneous strain distribution, as they are considered in this paper. While rate equation models are helpful to estimate the feasibility of Ge lasers, they fail to provide further hints for an appropriate device design since they lack spatial resolution.

In this paper we combine our recent insights into fabrication of strained Ge microstrips and the modeling of optical gain to perform a fully coupled 2D optoelectronic simulation using WIAS-TeSCA [22]. We follow an upscaling approach, which was successfully applied to multi-quantum well lasers before [23], [24]. Therefore, we consistently embed the gain computations into the simulation platform using an effective band model that accounts for the direct radiative recombination in the Γ-band, but assumes that charge transport of electrons is predominant in the *L*-band. This is done using an empirical gain model fitted to the microscopically computed gain, where it is crucial to fine-tune the band-gaps and the effective DOS masses in the simulations to the effective band structure from the tight binding calculations. We demonstrate the feasibility of this approach by comparing the modeled Fermi voltage with the one directly extracted from the computed material gain values. Using a version of WIAS-TeSCA that accounts for all these effects, we benchmark two different device designs with respect to their laser threshold and their modal stability and we study the impact of different loss mechanisms for the optimal design case. The novelty of our approach is the consistent combination of state-of-the art modeling for the optical gain of Ge with 2D optoelectronic device simulations.

2. Optoelectronic Modeling of Semiconductor Devices

The description of the carrier transport and the optical field can be restricted to a transverse cross section $\Omega \subset \mathbb{R}^2$ of the edge-emitter having a representative characteristic strain distribution. The evolution of charge carrier densities for electrons n and holes p is governed by drift-diffusion equations coupled to a Poisson equation for the electrostatic potential φ:

$$-\nabla \cdot (\varepsilon_0 \varepsilon_{\mathrm{r}} \nabla \varphi) = q(C - n + p) \tag{1a}$$

$$\frac{\partial n}{\partial t} - q^{-1} \nabla \cdot \mathbf{j}_{\mathrm{n}} = - R_{\mathrm{nr}} - R_{\mathrm{sp}} - R_{\mathrm{stim}} \tag{1b}$$

$$\frac{\partial p}{\partial t} + q^{-1} \nabla \cdot \mathbf{j}_{\mathrm{p}} = - R_{\mathrm{nr}} - R_{\mathrm{sp}} - R_{\mathrm{stim}}. \tag{1c}$$

Here C denotes the doping profile, q the elementary charge and $\varepsilon_0\varepsilon_r$ the permittivity. Moreover, R_{nr} contains all non-radiative recombination processes including Shockley–Read–Hall recombination–generation and Auger recombination, whereas $R_{sp} = C_{sp}(np - n_0p_0)$ is the rate of spontaneous radiative recombination, and R_{stim} is the recombination due to stimulated emission. The current densities $\mathbf{j}_n$ and $\mathbf{j}_p$ are defined by the gradients of the corresponding quasi Fermi-potentials φ_n and φ_p as

$$\mathbf{j}_n = -q\mu_n n\nabla\varphi_n \quad \text{and} \quad \mathbf{j}_p = -q\mu_p p\nabla\varphi_p \tag{2}$$

with μ_n and μ_p the electron and hole mobility. The dependence of the carrier densities for electrons and holes n and p on $\varphi_n, \varphi_p, \varphi$ is given by

$$n = N_c\,\mathcal{F}_{1/2}\left(\frac{q\varphi - q\varphi_n - E_c}{kT}\right) \quad \text{and} \quad p = N_v\mathcal{F}_{1/2}\left(\frac{E_v + q\varphi_p - q\varphi}{kT}\right) \tag{3}$$

where $\mathcal{F}_{1/2}$ is the Fermi–Dirac integral. With E_c, N_c, E_v, N_v we denote the band-edges and density of state (DOS) of the conduction and of the valence band, respectively. Each of these parameters depends on the specific material and on the strain. The rate of stimulated recombination reads

$$R_{stim} = \sum_j v_{g,j}g|\Xi_j|^2 S_j \tag{4}$$

where $v_{g,j}$ is the group velocity, g is the optical gain, $|\Xi_j|^2$ the modal intensity of the transverse mode j, and S_j the corresponding photon number.

A stable transverse waveguiding is usually assumed to describe optical modes in an edge-emitter cavity. For a longitudinally homogeneous power distribution the number of photons S_j in the mode j is balanced by the following photon rate equation

$$\dot{S}_j = v_{g,j}(2\Im m\beta_j - \alpha_c)S_j + \dot{S}_{sp,j}. \tag{5}$$

We have contributions from the net modal gain $2\Im m\beta_j$ and the positive spontaneous emission into the mode $\dot{S}_{sp,j}$. The photon number is related to the optical power emerging from one cavity facet by $P_j = \hbar\omega(1 - R_0)(v_{g,j}/L)S_j$. The term α_c comprises further loss mechanisms of the laser cavity. The complex-valued β_j and Ξ_j are eigenvalues and transverse eigenmodes of the waveguide equation with lasing frequency ω, which depending on polarization reads

$$\text{TE modes:} \quad \left[\nabla^2 + \frac{\omega^2}{c^2}\varepsilon_{opt}(\omega, \mathbf{r}) - \beta_j^2\right]\Xi_j(\mathbf{r}) = 0 \tag{6a}$$

$$\text{TM modes:} \quad \left[\nabla \cdot \frac{1}{\varepsilon_{opt}(\omega, \mathbf{r})}\nabla + \frac{\omega^2}{c^2} - \beta_j^2\right]H_{x,j}(\mathbf{r}) = 0 \tag{6b}$$

$$\text{and } \Xi_j(\mathbf{r}) = -\frac{\beta_j}{\omega\varepsilon_{opt}(\omega, \mathbf{r})}H_{x,j}(\mathbf{r}) = E_{y,j}(\mathbf{r}).$$

Here, the complex-valued dielectric function averaged over the longitudinal direction of the laser cavity is given by

$$\varepsilon_{opt}(\omega, \mathbf{r}) = \left(n_r(\omega, \mathbf{r}) + i\frac{c}{2\omega}\left[g(\omega, \mathbf{r}) - \alpha_{bg}(\mathbf{r})\right]\right)^2. \tag{7}$$

The dielectric function depends on the refractive index profile $n_r(\omega, \mathbf{r})$, the material gain $g(\omega, \mathbf{r})$ and the background absorption $\alpha_{bg}(\mathbf{r})$, which will be discussed in Section 3.2. For further details of this modeling, see [25].

TABLE 1

Band structure data for strained Ge layers as used for device simulation

strain layer	1	2	3	4	5	6	7	8	9	lateral	Si
$\varepsilon_{\mathrm{bi,j}}$[%]	0.35	0.39	0.44	0.48	0.53	0.57	0.61	0.66	0.7	≤ 0	-
E_g^L[meV]	655.6	653.6	651.6	649.6	647.5	645.3	643.0	640.7	638.3	665.6	1154
E_c[meV]	746.0	744.5	743.0	741.5	740.0	738.5	737.0	735.5	734.0	751.0	1169

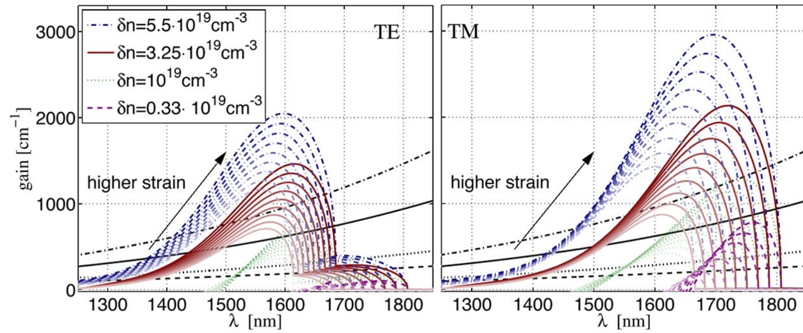

Fig. 1. Material gain for (left) TE and (right) TM polarization computed for four different excess carrier densities δn and nine increasing values of the biaxial strain (see Table 1) for n-doped Ge with a doping concentration $N_0 = 5 \times 10^{19}$ cm^{-3}. Higher values of the biaxial strain give higher values of the material gain, as indicated by the arrow. The free carrier absorption in Ge according to (10b) as a function of wavelength and excess carrier density δn is plotted as black lines. Both gain and free carrier absorption mostly increase with higher excess densities.

3. Modeling Optoelectronic Properties of Strained Germanium

The contribution of interband radiative recombination to the optical gain in the Ge active region was evaluated relying on the effective mass multi-valley model first presented in [15]. The model was validated against experimental data obtained by means of PL measurements in tensile strained Ge microstips [12]. Here, we only summarize the most relevant aspects of the model, referring to [15], [16] for a more detailed discussion. The near-gap band structure was calculated considering contributions from both the L and Γ valleys in the conduction band and from the heavy hole (HH), light hole (LH), and split off (SO) bands around the Γ point in the valence band. Modifications of these band-edge energies due to the biaxial strain field have been evaluated using deformation potentials from literature. To correctly describe effects related to the non-cubic symmetry of the strained material, we have assumed non-isotropic parabolic dispersion for the valence bands, characterized by in-plane and orthogonal effective masses whose values depend on the strain intensity [26]. Spectrally-resolved radiative recombination and absorption coefficients were calculated from Fermi's golden rule and using Fermi statistics for the carriers. The related quasi-Fermi energies were self-consistently calculated as a function of doping and excitation densities from the strain-dependent DOS assuming local charge neutrality. Contributions to the optical constants originating from both direct and phonon assisted radiative transitions were taken into account. To this aim, the semi-analytic expressions describing radiative recombination between bands with non-isotropic dispersions have been derived and numerically integrated [15]. Finally, since orbital redistribution between HH, LH, and SO states induced by the strain field also affects the intensity of the optical coupling with the conduction states, dipole matrix elements entering these expressions have been evaluated using a tight binding model with $sp^3d^5s^*$ basis orbitals [27] which fully captures this effect.

The device simulations reveal a local charge neutrality within the optically active Ge region. Therefore we study the optical gain as a function of the excess carrier density δn defining the electron and hole densities n, p by $n = N_0 + \delta n$, $p = \delta n$, where N_0 is the doping in the Ge. The resulting material gain spectra for different excess carrier densities δn, and a series of increasing biaxial strains according to Table 1 and TE/TM mode polarizations are shown in Fig. 1.

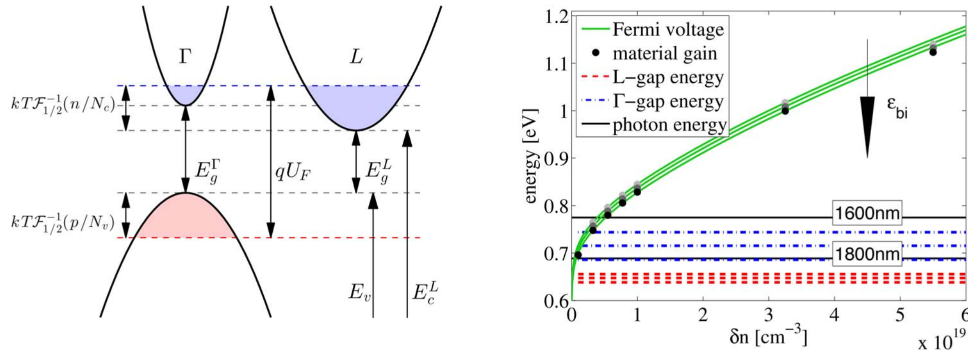

Fig. 2. (Left) Schematic band structure of moderately strained Ge. The valence band with the highest energy corresponds to light holes (LH). (Right) Variation of the Fermi voltage U_F as a function of excess carrier density δn as extracted from the microscopic computations (dark dots) in comparison with the effective model for the band-edge densities of state N_c^{eff}, N_v^{eff} used for device simulation (green lines) for strain $j = 1, 5, 9$ from Table 1. The corresponding Γ (blue) and L (red) gap energies are also displayed.

3.1 Band-Gaps, Density of States and Material Gain for Device Simulation

Microscopic gain calculations can be utilized for comprehensive device simulations based on semi-classical models, as described in Section 2, given that an appropriate upscaling of microscopically defined quantities to macroscopic equations of state was performed, cf. [23], [24]. This requires an accurate approximation of material gain as a function of carrier densities n and p only, but it also an approximation of the quasi-Fermi-level dependence $E_{Fn}(n), E_{Fp}(p)$ on the carrier densities themselves. The latter is important to match the same Fermi-voltage value, defined by $qU_F = E_{Fn} - E_{Fp}$, when calculated with the microscopic model and with the semi-classical expression for a given value of the excess carrier density δn. Using the L-valley band-edge as reference for the conduction band and the LH band-edge for the valence band, according to (3) the Fermi-voltage is defined by

$$qU_F = kT\mathcal{F}^{-1}_{1/2}(n/N_c) + kT\mathcal{F}^{-1}_{1/2}(p/N_v) + E_g^L(\varepsilon_{\text{bi}}) \quad (8)$$

where $E_g^L = E_c^L - E_v$ is the energy gap between the L-valley and the valence band; see Fig. 2. The effective band-edge DOS N_c and N_v for Ge are now adjusted in such a way, that the macroscopic dependence of the Fermi-voltage U_F on the excess carrier density fits the one obtained with the microscopic model, see right plot in Fig. 2. The effective value for the conduction band DOS is 1.5× larger than the reference value for unstrained Ge ($N_c^{\text{eff}} = 1.5 \times N_c^{\text{ref}}$), whereas the fit for the effective valence band DOS gives a value 4 × smaller ($N_v^{\text{eff}} = 1/4 \times N_v^{\text{ref}}$). The latter value is compatible with the reduced valence DOS mass of tensile strained Ge, used for the gain calculations reported in [15]. Since the material gain $g(\omega, \mathbf{r})$ has to vanish for $\hbar\omega = qU_F$ we used the zeros of the computed material gain spectra (see Fig. 1) to extract the microscopic dependence of the Fermi-voltage on the excess carrier density as a reference for fitting. The fitting procedure also provides slightly modified 'macroscopic' values for the L-valley band-gaps as summarized in Table 1. The consistency between the microscopic and "macroscopic" Fermi-voltage is of special importance for accurate device simulation, since the Fermi-voltage at the threshold determines the threshold voltage of the device and thus the actual value of the threshold current.

The density-dependence of the material gain shows a saturation behavior for larger values of the excess carrier density, see Fig. 3. In order to account for this effect and to accurately approximate the microscopic material gain data from in Fig. 1 for simulations with WIAS-TeSCA, we use the following modification of the usual $n \cdot p$ gain model by introducing a saturation term $1/(1 + \beta(np)^\gamma)$ in the gain formula

$$g(\omega, \delta n, \varepsilon_{\text{bi}}, N_0) = \kappa(\varepsilon_{\text{bi}}) \left(\exp\left(\frac{qU_F - \hbar\omega}{kT}\right) - 1 \right) \frac{np}{1 + \beta(np)^\gamma} \exp\left(\frac{-qU_F}{kT}\right) \quad (9)$$

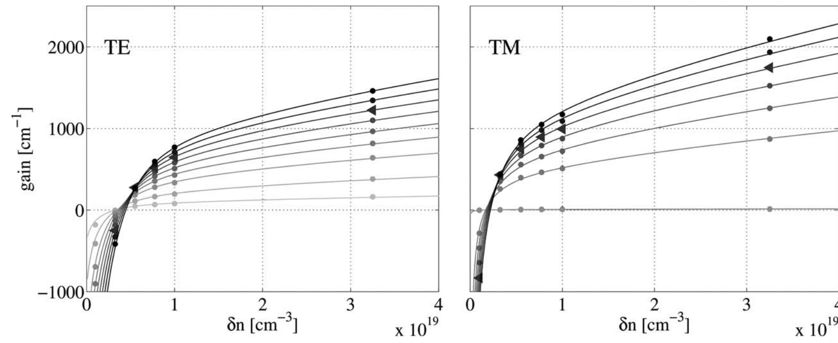

Fig. 3. Fit of the gain formula (9) to the material gain obtained by tight binding calculations at fixed wave length for TE mode (left) at $\lambda = 1620$ nm and for TM mode (right) at $\lambda = 1700$ nm for the strain values in Table 1. The data corresponding to $\varepsilon_{\text{bi}} = 0.61\%$ (triangles) were used to determine the exponent γ in (9).

TABLE 2

Coefficients for empiric gain fit (9) for different wavelengths and (*) TM and (†) TE polarization. The prefactors κ_j are measured in units of $\kappa \equiv \kappa_9$

λ[nm]	$\beta[\text{N}_0^{-2\gamma}]$	γ	$\kappa[\text{cm}^{-1}/N_0^2]$	$\kappa_1[\kappa]$	$\kappa_2[\kappa]$	$\kappa_3[\kappa]$	$\kappa_4[\kappa]$	$\kappa_5[\kappa]$	$\kappa_6[\kappa]$	$\kappa_7[\kappa]$	$\kappa_8[\kappa]$
1650*	$1.00 \cdot 10^6$	0.58	$7.26 \cdot 10^{21}$	0.38	0.53	0.64	0.72	0.80	0.86	0.91	0.96
1700*	$1.75 \cdot 10^{15}$	0.66	$6.40 \cdot 10^{30}$	$6 \cdot 10^{-3}$	$6 \cdot 10^{-3}$	$7 \cdot 10^{-3}$	0.43	0.61	0.74	0.84	0.93
1720*	$5.44 \cdot 10^6$	0.69	$1.46 \cdot 10^{22}$	$4 \cdot 10^{-3}$	$6 \cdot 10^{-3}$	$6 \cdot 10^{-3}$	$7 \cdot 10^{-3}$	0.42	0.63	0.78	0.90
1570†	5.53	0.72	$1.50 \cdot 10^{17}$	0.57	0.64	0.70	0.76	0.81	0.87	0.92	0.96
1620†	13.4	0.71	$1.50 \cdot 10^{17}$	0.11	0.26	0.43	0.55	0.66	0.75	0.84	0.92
1640†	75.8	0.67	$5.36 \cdot 10^{17}$	0.10	0.12	0.13	0.14	0.49	0.65	0.78	0.89

where $g(\omega, \mathbf{r}) = g(\omega, \delta n(\mathbf{r}), \varepsilon_{\text{bi}}(\mathbf{r}), N_0)$, and $U_F(\mathbf{r}) = U_F(\delta n(\mathbf{r}), \varepsilon_{\text{bi}}(\mathbf{r}))$ depend on space. For $qU_F > \hbar\omega$ the gain is positive, otherwise there is absorption. For any fixed wavelength, polarization, and doping concentration, we determine optimal values of β and γ and compute the corresponding $\kappa(\varepsilon_{\text{bi}})$ for all the strained layers (see Table 2). In practice, we expect the laser to operate near the threshold at qU_F greater but close to $\hbar\omega$. Therefore the fit with (9) needs to be accurate in the vicinity of $qU_F = \hbar\omega$. In Fig. 3 we show the fit of the microscopically calculated gain to the gain model (9) for both TE and TM polarization for the nine values of biaxial strain from Table 1 at one particular wavelength and doping concentration $N_0 = 5 \times 10^{19}$ cm^{-3} as a function of excess carrier density. The parameter β serves mainly as a scaling parameter, while the parameter γ describes the deviation from the $n \cdot p$ behavior, namely $g(n, p) \approx (np)^{1-\gamma}$, and accounts for the actual joint band densities of state as calculated in the microscopic model.

As a reference to determine the optimal values for β, γ the gain curve for $(\varepsilon_{\text{bi}})_{j=7} = 0.61\%$ is used, whereas the values of $\kappa(\varepsilon_{\text{bi}})$ are adjusted for each strain value separately after fixing β, γ. The fitted gain curves in Fig. 3 are displayed for the lasing wavelength corresponding to the minimum threshold current for a device with a value of $\alpha = 80$ cm^{-1} for the extra losses (see Section 4.4). Fig. 3 also allows us to evaluate the excess carrier density needed to obtain positive gain. It is approximately 5×10^{18} cm^{-3} for TE polarization and 2×10^{18} cm^{-3} for TM polarization. Based on this observation and owing to the general tendency for TM polarization to achieve higher gain values at given excess carrier density, it can be expected that the laser emission will favor TM polarization.

3.2 Free Carrier Absorption

The absorption of light related to the presence of free carriers represents an important loss mechanism when high excitation densities and/or heavy doping are used in the active region of the device. Hole and electron contributions to the free carrier absorption (FCA) in heavily doped *n*-type [28]–[30] and *p*-type [31] Ge have been first studied in the Sixties.

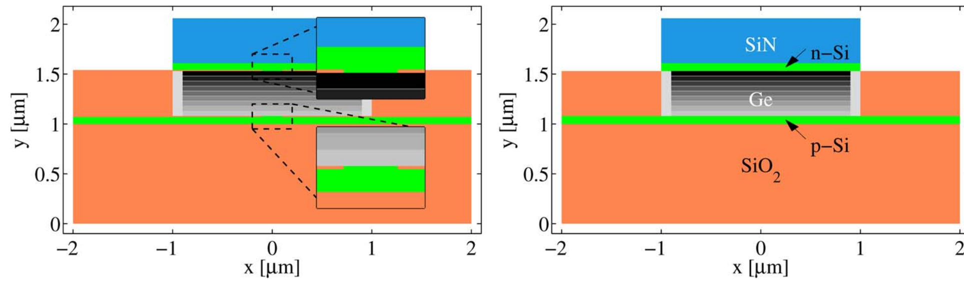

Fig. 4. Simulation geometry for (left) the aperture design and (right) the standard device design. The device is made of SiN (blue), SiO_2 (orange), poly-Si (green), and Ge (gray). The nine shades of gray represent the values of the biaxial tensile strain (see Table 1) increasing from bottom to top. Notice that the Ge lateral regions are under compressive biaxial strain indicated by the light gray regions. The insets in the left panel magnify the oxide apertures used to inject the carriers into the central region.

More recently, Liu [32] proposed a wavelength-dependent empirical relation to fit these historical data, assuming a linear dependence on the total (i.e., equilibrium plus excess) electron and hole carrier densities. Carrol *et al.* [33] reported measurements of free electron and hole cross sections in heavily doped Ge at the direct band-gap photon energy. Quite remarkably, the hole cross section was estimated to be larger by a factor 12$\times$ with respect to the electronic one, probably due to the presence of intervalence scattering channels with no analogous counterpart in the conduction band. Carrol *et al.* [33] also stated that the measured cross sections are in reasonable agreement with Spitzer *et al.* [28] as well as with Newman and Tyler [31]. On this basis, Boucaud *et al.* [6] critically compared the results of Carrol *et al.* [33] and Liu *et al.* [32]. They concluded that [32] probably overestimated the electronic contribution by a factor of about two while, at the same time, underestimated the hole contribution by approximately the same factor. However, at a closer look, the agreement between the hole cross section estimated by Carroll and the finding of Newman and Tyler [31] only hold for large carrier densities (5×10^{19}–1×10^{20} cm^{-3}). At lower hole concentrations the cross sections by Carrol *et al.* significantly overestimate the values measured by Newman and Tyler. From the above discussion, although some uncertainty remains, it seems reasonable to model the free carrier absorption relying on a modified version of the formula reported by Liu and coworkers [32]. More precisely, since in the present paper the hole concentration is of order 10^{18} cm^{-3}, following Boucaud *et al.* [6] and Carrol *et al.* [33], we divide the electron contribution to the FCA estimated by Liu *et al.* by two, while we keep their expression for the contribution by holes unchanged. For typical hole concentrations observed in our simulations, Liu's formula for the FCA absorption seems a conservative fit of the absorption measurements reported by Newman and Tyler [31]. In conclusion, we describe the FCA contribution in Ge to the optical background losses entering the dielectric function (7) by

$$\alpha_{\mathrm{bg}}(\mathbf{r}) = f_{\mathrm{cn}}^{\mathrm{Ge}} n + f_{\mathrm{cp}}^{\mathrm{Ge}} p \tag{10a}$$

with the coefficients

$$f_{\mathrm{cn}}^{\mathrm{Ge}} = 1.7 \times 10^{-25}\ \mathrm{cm}^2 \cdot (\lambda/[\mathrm{nm}])^{2.25}, \quad f_{\mathrm{cp}}^{\mathrm{Ge}} = 3.25 \times 10^{-25}\ \mathrm{cm}^2 \cdot (\lambda/[\mathrm{nm}])^{2.43}. \tag{10}$$

4. Two-Dimensional Simulations of an Electrically Pumped Ge-on-Si Laser

4.1 Device Structure and Simulation Setup

In this section we use WIAS-TeSCA to compare two different designs for 400 μm long Ge-on-Si edge-emitting lasers with lateral current injection. The material composition of the two device designs is shown in Fig. 4 as a transverse cross section. The growth direction is y. The layer structure in the active region consists of a 450 nm thick, n-doped, strained Ge layer

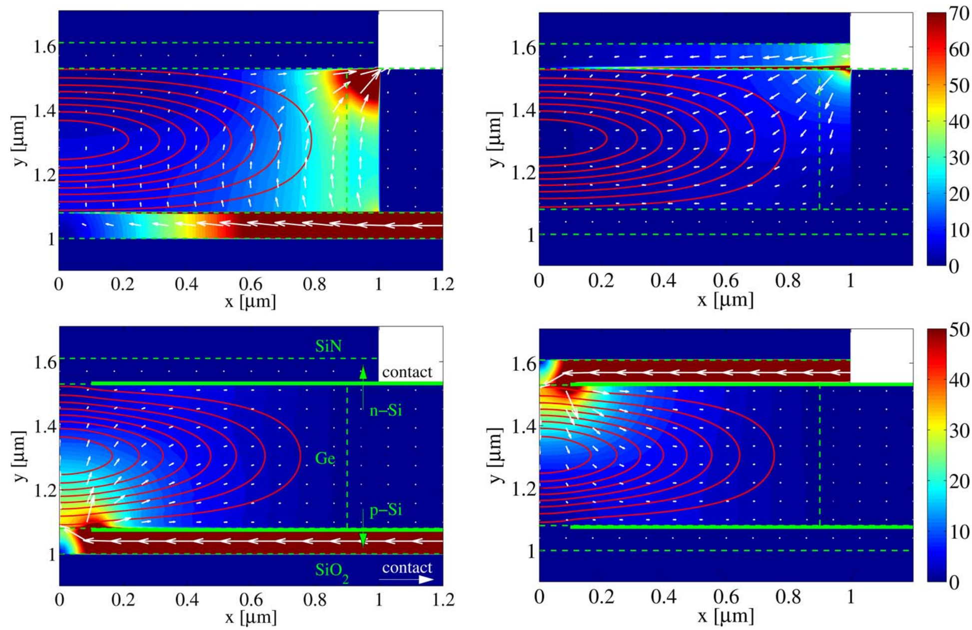

Fig. 5. Current density and current density vector field (white arrows) for the (top) standard design and the (bottom) aperture design. (Left) Hole currents. (Right) Electron currents. The isolines of the mode intensity $|\Xi|^2$ of the fundamental mode for TM polarization are shown in red. The results are shown for the wavelength at the minimum threshold corresponding to $\lambda = 1708$ nm for aperture and $\lambda = 1704$ nm for standard design, both for an optical power $P = 0.05$ mW with $\alpha = 80$ cm^{-1} extra losses. The colored background indicates the distribution of Joule heating effects by showing the magnitude of the current density vector $|\mathbf{j}_{n/p}|$ in units of kA/cm^2.

(gray-shaded) sandwiched between two highly doped Si layers (green) acting as contact layers (bottom: p-doped, top: n-doped). The left panel of Fig. 4
shows what we call the *aperture design*. It contains a 10 nm thick oxide blocking layer that partially isolates the Ge from the Si contacts, with carriers free to flow only through a 200 nm wide gap located at the center (see insets in Fig. 4). The *aperture* configuration could be realized exploiting the recently developed *epitaxial lateral overgrowth* technique, allowing for the local fabrication of GeOI strips [34].

In the *standard design* shown in the right panel of Fig. 4 these blocking layers are absent. The Si contacts are 80 nm thick in the standard device and 70 nm thick in the aperture device. The 500 nm thick SiN top-layer (blue) induces a tensile strain in the Ge block. The strain field distribution for similar structures has been investigated in [12], [14] and it is here used to model the structural properties of the Ge microstrip. The darkness of the gray hue in Fig. 4 encodes the amount of tensile biaxial strain, which is assumed to linearly increase from bottom to top. This behavior is approximated in our device simulations by 9 Ge layers of 50 nm thickness each, with constant strain corresponding to the values $\varepsilon_{\mathrm{bi},j=1..9}$ in Table 1. The lateral regions of compressive strain observed in the experiment, have an increased band-gap and hence, at high n-doping, act like a small barrier for the holes, see Fig. 5 (right). But also the gap between the Γ- and the L-valley is increased and thereby inhibits the optical gain. In order to reflect this feature in the electronic model we use the material data of Ge with increased band-edge energies and band-gaps as given in Table 1. The structure is realized on a SiO_2 substrate (SOI) (orange), set up with 4 μm width and 1 μm thickness in the simulation domain. We point out that SOI can be replaced by bulk Si substrate in order to reduce the thermal resistance of the device, as described in [17], at the expenses of a lesser confinement of the optical mode.

The material parameters used for the simulations and in the subsequent discussion are summarized in Table 3. For Si these are standard values for band-gap, DOS and mobility. As a reference energy for the strain-dependent conduction bands E_c, we choose a microscopically

TABLE 3

Values of the material parameters used for device simulation

Parameter	Value	Parameter	Value	Parameter	Value
mobilities:		electrostatic permittivity:		refractive index:	
$\mu_n(\mathrm{Ge})$	$3900\ \mathrm{cm^2/Vs}$	$\varepsilon_r(\mathrm{Si})$	11.9	$n_r(\mathrm{Si})$	3.4
$\mu_p(\mathrm{Ge})$	$1900\ \mathrm{cm^2/Vs}$	$\varepsilon_r(\mathrm{Ge})$	16.2	$n_r(\mathrm{Ge})$	4.2
$\mu_n(\mathrm{Si})$	$1400\ \mathrm{cm^2/Vs}$	$\varepsilon_r(\mathrm{SiO_2})$	3.8	$n_r(\mathrm{SiO_2})$	1.5
$\mu_p(\mathrm{Si})$	$450\ \mathrm{cm^2/Vs}$	$\varepsilon_r(\mathrm{SiN})$	7.5	$n_r(\mathrm{SiN})$	2.0
DOS:		SRH lifetimes:		Doping:	
$N_c^{\mathrm{ref}}(\mathrm{Ge})$	$1.028 \times 10^{19}\mathrm{cm^{-3}}$	$\tau_n(\mathrm{Ge/Si}), \tau_p(\mathrm{Ge/Si})$	$1 \times 10^{-7}\ \mathrm{s}$	Si : n-type	$2 \times 10^{20}\mathrm{cm^{-3}}$
$N_v^{\mathrm{ref}}(\mathrm{Ge})$	$0.5 \times 10^{19}\mathrm{cm^{-3}}$	Auger coefficients:		Si : p-type	$2 \times 10^{20}\mathrm{cm^{-3}}$
$N_c^{\mathrm{eff}}(\mathrm{Ge})$	$1.5 \times N_c^{\mathrm{ref}}(\mathrm{Ge})$	$C_n(\mathrm{Ge/Si})$	$7 \times 10^{-32}\ \mathrm{cm^6/s}$	Ge : n-type	$5 \times 10^{19}\mathrm{cm^{-3}}$
$N_v^{\mathrm{eff}}(\mathrm{Ge})$	$0.25 \times N_v^{\mathrm{ref}}(\mathrm{Ge})$	$C_p(\mathrm{Ge/Si})$	$3 \times 10^{-32}\ \mathrm{cm^6/s}$	group velocity:	
$N_c(\mathrm{Si})$	$2.82 \times 10^{19}\mathrm{cm^{-3}}$	spontaneous emission:		v_g	3.6
$N_v(\mathrm{Si})$	$1.83 \times 10^{19}\mathrm{cm^{-3}}$	$C_{\mathrm{sp}}(\mathrm{Ge/Si})$	$1 \times 10^{-12}\ \mathrm{cm^3/s}$		

calculated profile for the L-valley; see Table 1. The corresponding band-gaps and effective conduction and valence band DOS parameters N_c^{eff}, N_v^{eff} have been obtained by the upscaling procedure described in Section 3.1; see Tables 1 and 3. For the Shockley–Read–Hall recombination carrier lifetimes τ_n, τ_p and the Auger coefficients C_n, C_p in Ge we have chosen typical literature values used for modeling of Ge lasers so far: $\tau_n = \tau_p = 100$ ns and $C_n = 3 \times 10^{-32}$ cm^6/s, $C_p = 7 \times 10^{-32}$ cm^6/s, cf. [10], [18], [32]. The rate for the spontaneous emission has been estimated to $C_{sp} = 1 \times 10^{-12}$ cm^3/s using an Arrhenius law interpolating between the values for the Γ and L-valleys, $R_\Gamma = 1.3 \times 10^{-10}$ cm^3/s and $R_L = 5.1 \times 10^{-15}$ cm^3/s, see [32] and [30], [31] therein. Here, the average energy difference $E_{\Gamma L}$ defines the activation energy. For the carrier mobilities in Ge we assumed standard values for unstrained bulk material. For the electrostatic permittivity and the refractive index in the materials also literature values are used. The temperature is constant at $T = 300$ K.

4.2 Optoelectronic Performance of Designs

Typical current distributions above lasing threshold for both designs are depicted in Fig. 5. The upper panel of the figure shows that the standard device design leads to a spatially inhomogeneous current injection into Ge, in particular favoring hole currents directly towards the n-contact without passing the mode maximum located in the center of the active region. At high voltage this leads to a leakage current close to the compressive region. This 2D transport phenomenon results from the lateral current injection increasing the threshold current (see Fig. 6) and, thus, limits the efficiency of the device. The right panel of Fig. 6 also shows that the standard design favors excited modes rather than the fundamental mode for higher output powers. Despite of the strain engineering, the threshold current of the standard device with $\alpha = 80$ cm^{-1} extra losses is only reduced by a factor 1/2 compared to the MIT design.

In order to improve the carrier injection into the fundamental mode, we introduce an oxide aperture for the current as electron and hole blocking layers (see the left panel and insets in Fig. 4). Here, these oxide layers form a 200 nm wide aperture for the currents, as can be seen in the lower panel of Fig. 5. The use of oxide aperture is a common technique to optimize the current injection in VCSEL devices. Fig. 6 shows that by this optimization of the current injection in the aperture design we reduce the threshold current density by almost a factor 4×, which is an order of magnitude smaller than that reported in [4]. This demonstrates the high potential of using higher strains together with device optimization in order to reduce the threshold considerably.

According to [25], we can study the mode selection by using lowest order perturbation theory, which gives for the modal net-gain

$$2\Im m\beta_j = \int \frac{\omega n_r}{c\Re e\beta_j}(g - \alpha_{bg})|\Xi_j|^2 dA \Big/ \int |\Xi_j|^2 dA. \qquad (11)$$

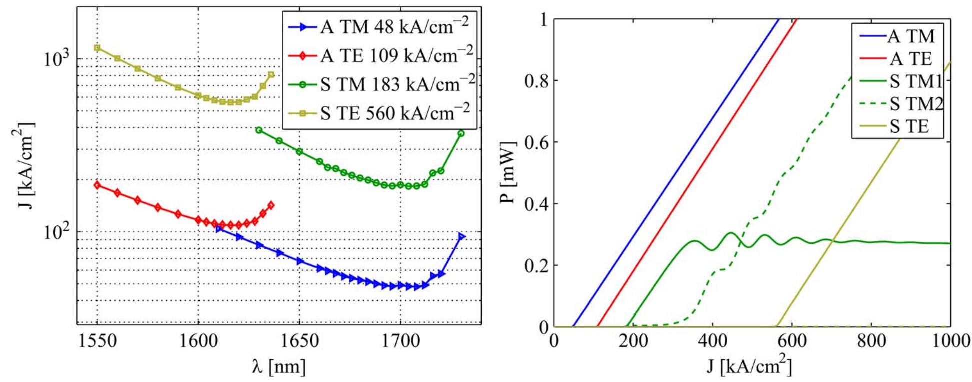

Fig. 6. (Left) Dependence of the threshold current as a function of the wave length for both device geometries (A: aperture, S: standard) for an extra loss value $\alpha = 80$ cm^{-1}. The values of the threshold current at the minima are given in the legend. (Right) Corresponding power–current characteristics for the two devices at minimal threshold wave length for TE and TM, respectively. Using the contact area $A = 6.4 \times 10^{-3}$ cm^2, the threshold current densities of 48, 109, 183, and 560 kA/cm^{-2} correspond to device currents of 30, 70, 117, and 358 mA, respectively.

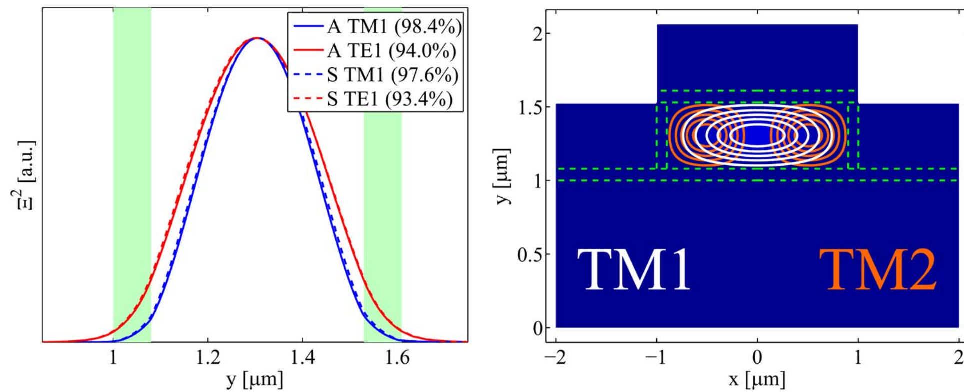

Fig. 7. (Left) Modal intensity profile Ξ_j^2 for standard (S) and aperture (A) design for TM1 and TE1 as obtained as eigenmodes of the Helmholtz problem. The numbers in the legend are the optical confinement factors of the optically active Ge wave guide. (Right) Cross-sectional modal intensity for TM1 and TM2.

For the wavelengths and geometry under consideration, we have $\omega n_r / c \Re e \beta_j \approx 1$. The mode selection and the threshold current are influenced by the modal net-gain balancing a positive contribution from the material gain with a negative contribution from modal losses caused by free carrier absorption in Ge and in the highly doped poly-Si contacts.

For strain values in the 0.35–0.7% range, much higher material gain is predicted for TM than for TE; see Fig. 1. The optical modes of both designs feature an optical confinement factor in the Ge waveguide of about 98% for TM and about 94% for TE polarization. Hence, the modal gain for TM is larger than for TE. Moreover, the additional modal losses due to the overlap of the squared eigenfunction $|\Xi_j|^2$ with the highly doped Si-contact layers [green stripes in Fig. 7 (left)] is considerably larger for TE than for TM. Our devices clearly favor TM emission as demonstrated in Fig. 6. In contrast, the MIT-device uses vertical carrier injection through thick, highly doped Si-poly layers. It is reported to operate in the TE-mode [4], [21], which in [21] is explained by high additional losses in the contact layers. For their design these losses are much higher for TM than for TE polarization (see discussion in Section 4.4).

The current-power characteristics for the *standard* design in Fig. 6 shows a switching from TM1 to the first excited mode TM2. This happens for larger currents of about 500 kA/cm^2

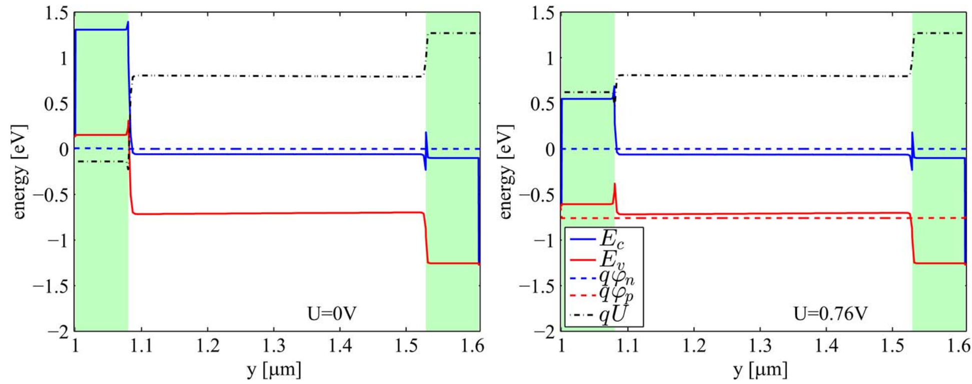

Fig. 8. Variation of the band-edges, quasi Fermi-levels and of the electrostatic potential (U) as a function of the y position shown at the center ($x = 0$) of the device for two bias conditions: (Left) Equilibrium at $U = 0$ V. (Right) Slightly above threshold at $U = 0.76$ V corresponding to a optical output power of $P = 0.05$ mW. x,y-coordinates as in Fig. 4.

near the threshold. This behavior can be explained by the fact that, in particular for holes, the current is localized near the lateral boundaries of the Ge layer as shown in Fig. 5. At higher optical output powers the electron and hole currents need to compensate the stimulated recombination (4) proportional to $g|\Xi_j|^2$. If the current density is localized near the lateral boundaries, then this will favor an excitation of higher modes (see contour of modes in Fig. 7). In contrast, the *aperture* design reduces the current spreading by concentrating the electron and hole currents in the central region of the Ge having two effects: It reduces the "leakage" current which does not contribute to stimulated recombination and it stabilizes the fundamental mode (see Fig. 5).

4.3 Influence of Inhomogeneous Strain Distribution

The SiN stressor technique can be used to increase the tensile strain in the Ge microstrips in order to achieve higher material gain than in a purely thermal strained Ge/Si layer. However, the spatially inhomogeneous strain profile results in an increasing strain from bottom to top as shown in Fig. 4. The related deformation influences both, the effective band-gap (L-valley to LH) and the relative position of the conduction band-edge energy resulting in a slightly decreasing size of the band-gap from bottom to top and a shift of L-valley band-edge towards lower energies, cf. Table 1. The reduced energy difference between L and Γ-valley results in much higher material gain, see Fig. 3. Moreover, due to the high n-doping, the band-gap shrinkage induces titled band-edges for the holes; see Fig. 8. The tilted band-edges in turn lead to a slightly increasing hole density from bottom to top; see Fig. 1 and Fig. 9. Thus both, the material gain coefficient and the excess carrier density δn defined by the hole density are increasing from bottom to top and lead to a strong variation of the local material gain across the Ge layer; see Fig. 9.

The resulting material gain profile enters the modal gain (11) by the overlap with the profile of the modal intensity. As one can see, even for the optimal design with $\lambda = 1708$ nm not all layers contribute to the modal gain. The modal intensity is concentrated around the central layers, see Fig. 9, whereas the material gain attains its maximum in the top layers. As a consequence, only a fraction of the available material gain contributes to the modal gain. This property is a disadvantage of the stressor device concept in comparison to the MIT device structure. The MIT design is assumed to have lower but homogeneous strain distribution implying a constant material gain entirely contributing to the modal gain.

In return, for our design this difference opens up a new possibility for a further reduction of the threshold current by optimization of the overlap between material gain and modal intensity. We conclude therefore that device concepts based on strain gradients also require an overlap engineering in order to achieve the full benefit of a higher strain.

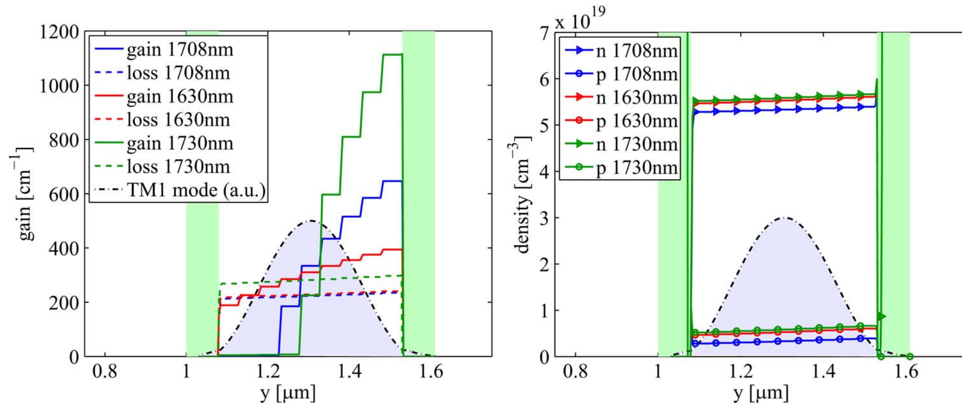

Fig. 9. (Left) Profiles for material gain and free carrier absorption and (right) carrier densities for different wave lengths and $\alpha = 80$ cm^{-1} as a function of the y position shown at the center ($x = 0$) of the device; cf. Fig. 9. The TM1 modal intensity is also represented as the shaded area.

4.4 Variation of the Losses

The cavity losses α_c in (5) are decomposed into output losses α_o of the laser cavity and into extra losses α, where

$$\alpha_c := \alpha_o + \alpha \text{ with } \alpha_o = \frac{1}{2L}\ln\left(\frac{1}{R_0 R_1}\right). \tag{12}$$

With a cavity length $L = 400$ μm and facet reflectivities $R_0 = R_1 = 0.9$ this results in rather small output losses of $\alpha_o = 3$ cm^{-1}. The extra losses α consist of the longitudinal scattering losses and the losses by the FCA in the highly doped Si. The latter can be estimated by

$$\alpha_{FCA,Si} = \frac{\int_{\Omega_{Si}} (f_{cn}^{Si} n + f_{cp}^{Si} p)|\Xi_j|^2 \, dA}{\int |\Xi_j|^2 \, dA} \approx \frac{2 \cdot 10^{20} \text{ cm}^{-3}}{2} (f_{cn}^{Si} + f_{cp}^{Si}) \frac{\int_{\Omega_{Si}} |\Xi_j|^2 \, dA}{\int |\Xi_j|^2 \, dA} = \alpha_{fc,Si}(1 - F)$$

where F is the optical confinement factor and $\alpha_{fc,Si}$ the effective absorption related to the doping concentration. The factor 1/2 distributes the overlap with the Si-layer equally between the 2×10^{20} cm^{-3} n-doped and p-doped layer. An extrapolation formula provided by Isenberg & Warta [35] is used to approximate f_{cn}^{Si}, f_{cp}^{Si} for highly doped Si at $\lambda = 1700$ nm and a prefactor of about $\alpha_{fc,Si} = 3000$ cm^{-1} is obtained. For the confinement factor of 98.4% for the TM1 mode in the aperture design, one gets $\alpha_{FCA,Si} = 48$ cm^{-1}. A typical value for the longitudinal scattering losses is 20 cm^{-1}. Thus, a value of $\alpha = 80$ cm^{-1} for the extra losses used for the comparison between aperture and standard design is quite realistic for TM polarization. Due to the lower optical confinement factor of 94.4% for the TE1 mode in the standard design a higher value of $\alpha_{FCA,Si} = 168$ cm^{-1} is obtained. In other words, we underestimate the FCA in Si, and thereby, we also underestimate the threshold current in a simulation with $\alpha = 80$ cm^{-1} for TE polarization. Note that for the chosen length there is still the potential to decrease the reflectivities in order to increase the optical output power in exchange for higher losses. Even with reflectivities of $R_0 = R_1 = 0.36$ relative to the Ge/air interface we get $\alpha_o = 26$ cm^{-1} as a subdominant contribution compared to free carrier absorption in the Si.

Fig. 10 shows a series of simulations for the aperture design with TM polarizations and increasing losses $\alpha = \{40, 80, 160, 320\}$ cm^{-1}. One can clearly see the increase of the threshold density with increasing losses, but also the tendency for the optimal wavelength to be shifted toward shorter wavelength, i.e., a blueshift. This is also in accordance with experimental observations by the MIT group [21]. Similar to the comparison between standard and aperture design one can observe stabilization of higher modes with higher losses, now even at low

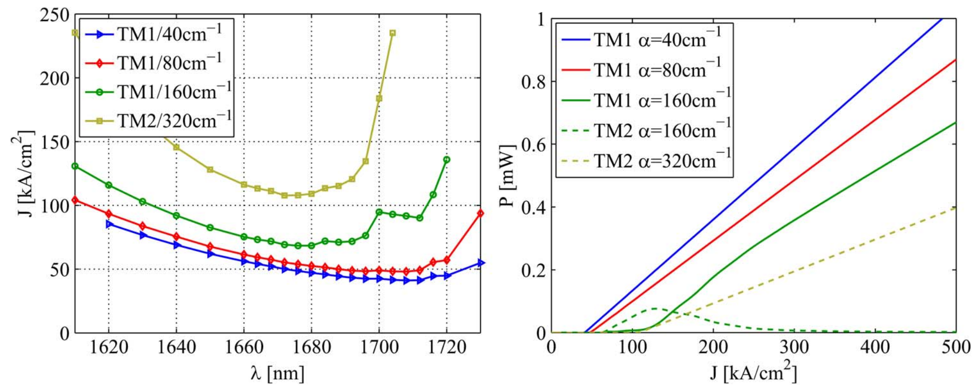

Fig. 10. (Left) Dependence of the threshold current as a function of the wave length for an aperture design for different values of the extra losses. (Right) Corresponding power–current characteristics at minimal threshold wave length. Notice the onset of the TM2 mode for low currents for $\alpha = 160$ cm^{-1} and the switch to stable TM2 emission for $\alpha = 320$ cm^{-1}.

output powers. This is because high losses force the laser to operate in high-gain regions. Thereby recombination $g|\Psi_j|^2$ will locally deplete charges and favor excited modes, which are more spread-out. We notice that, for losses $\alpha > 160$ cm^{-1}, this effect can not be prevented even in the improved aperture design. This clearly shows that design optimization towards mode stability also depends on the desired operation parameters (loss, output power) of the laser.

5. Conclusion

A drift-diffusion approach for modeling and simulation of edge-emitting lasers based on strained Ge microstrips is presented and uses microscopically calculated data for the material gain. To utilize the microscopic gain calculations for the semi-classical device simulation, a specific gain model for strained Ge was developed. The parameters of this model are obtained by a fitting procedure using the computed gain spectra. The important equivalence between microscopic and macroscopic Fermi-voltages for given values of the excess carrier density is achieved by a careful adjustment of the effective band-edge DOS for Ge.

This calibrated model has been used to study the optoelectronic performance of a laser design which uses SiN as a stressor material on top of the optically active Ge region to achieve higher values of the material gain. Simulations for this design, require a lateral current injection. They showed high "leakage" currents along the lateral boundaries not contributing to stimulated recombination. This 2D carrier transport phenomenon limits the benefit of the increased material gain to reduce the threshold current in comparison to device concepts with vertical carrier injection and lower, but homogeneous strain distribution. In order to reduce the threshold current an aperture design is introduced. It improves the carrier injection into the fundamental optical mode. For the aperture design the simulations predict a threshold current which is 4$\times$ lower than for the standard design demonstrating the high potential of optoelectronic optimization towards lower threshold in the high-strain setting.

An analysis of the modal gain showed that the inhomogeneous strain distribution, assumed to linearly increase from 0.35% (bottom) to 0.7% (top) in our case, leads to a strong variation of the available material gain favoring higher values of the strain at the top of the Ge region. This behavior can be explained by the variation of the energy difference between Γ- and L-valley influencing the available electrons in the Γ-valley and by the localization tendency of the holes in regions with smaller band-gaps in the highly n-doped Ge. Since the modal intensity is concentrated in the center of the Ge layer, only a fraction of the available material gain contributes to the modal gain due to the reduced overlap. This provides another way to optimize the optoelectronic performance of the proposed Ge emitter device by overlap engineering.

Acknowledgment

The authors would like to thank H. Gajewski, U. Bandelow, and H.-J. Wünsche for many fruitful discussions and helpful remarks.

References

[1] N. Daldosso and L. Pavesi, "Nanosilicon photonics," *Laser Photon. Rev.*, vol. 3, no. 6, pp. 508–534, 2009.
[2] D. Liang and J. E. Bowers, "Recent progress in lasers on silicon," *Nature Photon.*, vol. 4, no. 8, pp. 511–517, 2010.
[3] J. Liu, X. Sun, R. Camacho-Aguilera, L. C. Kimerling, and J. Michel, "Ge-on-Si laser operating at room temperature," *Opt. Lett.*, vol. 35, no. 5, pp. 679–681, 2010.
[4] R. E. Camacho-Aguilera *et al.*, "An electrically pumped germanium laser," *Opt. Exp.*, vol. 20, no. 10, pp. 11 316–11 320, May 2012.
[5] B. Dutt *et al.*, "Roadmap to an efficient germanium-on-silicon laser: Strain versus n-type doping," *IEEE Photon. J.*, vol. 4, no. 5, pp. 2002–2009, Oct. 2012.
[6] P. Boucaud *et al.*, "Recent advances in germanium emission," *Photon. Res.*, vol. 1, no. 3, pp. 102–109, Oct. 2013.
[7] Y. Huo *et al.*, "Strong enhancement of direct transition photoluminescence with highly tensile-strained ge grown by molecular beam epitaxy," *Appl. Phys. Lett.*, vol. 98, no. 1, Jan. 2011, Art. ID. 011111.
[8] V. D'Costa, Y.-Y. Fang, J. Tolle, J. Kouvetakis, and J. Menendez, "Tunable optical gap at a fixed lattice constant in group-IV semiconductor alloys," *Phys. Rev. Lett.*, vol. 102, no. 10, Mar. 2009, Art. ID. 107403.
[9] S. Wirths *et al.*, "Lasing in direct-bandgap GeSn alloy grown on Si," *Nature Photon.*, vol. 9, pp. 88–92, 2015.
[10] J. R. Jain *et al.*, "A micromachining-based technology for enhancing germanium light emission via tensile strain," *Nature Photon.*, vol. 6, no. 6, pp. 398–405, 2012.
[11] M. Sess *et al.*, "Analysis of enhanced light emission from highly strained germanium microbridges," *Nature Photon.*, vol. 7, no. 6, pp. 466–472, 2013.
[12] G. Capellini *et al.*, "Tensile Ge microstructures for lasing fabricated by means of a silicon complementary metal–oxide–semiconductor process," *Opt. Exp.*, vol. 22, no. 1, pp. 399–410, Jan. 2014.
[13] G. Capellini, G. Kozlowski, Y. Yamamoto, M. Lisker, and C. Wenger, "Strain analysis in SiN/Ge microstructures obtained via Si-complementary metal oxide semiconductor compatible approach," *J. Appl. Phys.*, vol. 113, no. 1, 2013, Art. ID. 013513.
[14] G. Chahine *et al.*, "Strain and lattice orientation distribution in SiN/Ge CMOS compatible light emitting microstructures by quick X-ray nano-diffraction microscopy," *Appl. Phys. Lett.*, vol. 106, no. 7, Feb. 2015, Art. ID. 071902.
[15] M. Virgilio, C. L. Manganelli, G. Grosso, G. Pizzi, and G. Capellini, "Radiative recombination and optical gain spectra in biaxially strained *n*-type germanium," *Phys. Rev. B*, vol. 87, Jun 2013, Art. ID. 235313.
[16] M. Virgilio, C. L. Manganelli, G. Grosso, T. Schroeder, and G. Capellini, "Photoluminescence, recombination rate, and gain spectra in optically excited n-type and tensile strained germanium layers," *J. Appl. Phys.*, vol. 114, no. 24, Dec. 2013, Art. ID. 243102.
[17] G. Capellini *et al.*, "CMOS-fabricated tensile Ge microstructures: Towards an edge-emitting laser," in *Proc. 7th ISTDM*, 2014, pp. 133–134.
[18] W. Chow, J. Kabuss, and A. Carmele, "Analysis of lasing from direct transition in Ge-on-Si," *IEEE J. Sel. Topics Quantum Electron.*, vol. 19, no. 4, Jul. 2013, Art. ID. 1502309.
[19] X. Sun, J. Liu, L. Kimerling, and J. Michel, "Toward a germanium laser for integrated silicon photonics," *IEEE J. Sel. Topics Quantum Electron.*, vol. 16, no. 1, pp. 124–131, Jan 2010.
[20] J. Liu *et al.*, "Ge-on-Si optoelectronics," *Thin Solid Films*, vol. 520, no. 8, pp. 3354–3360, Feb. 2012.
[21] R. E. Camacho-Aguilera, "Ge-on-Si laser for silicon photonics," Ph.D. dissertation, Mass. Inst. Technol., Cambridge, MA, USA, 2013.
[22] H. Gajewski and R. Nürnberg, "WIAS-TeSCA: Two- and three-dimensional semiconductor analysis package." [Online]. Available: https://www.wias-berlin.de/software/tesca/
[23] U. Bandelow, R. Hünlich, and T. Koprucki, "Simulation of static and dynamic properties of edge-emitting multi quantum well lasers," *IEEE J. Sel. Topics Quantum Electron.*, vol. 9, no. 3, pp. 798–806, May/Jun. 2003.
[24] T. Koprucki, H.-C. Kaiser, and J. Fuhrmann, "English electronic states in semiconductor nanostructures and upscaling to semi-classical models," in *Analysis, Modeling, and Simulation of Multiscale Problems*, A. Mielke, Ed. Berlin, Germany: Springer-Verlag, 2006, pp. 365–394.
[25] U. Bandelow, H. Gajewski, and R. Hünlich, "Fabry–Perot lasers: Thermodynamics-based modeling," in *Optoelectronic Devices: Advanced Simulation and Analysis*. New York, NY, USA: Springer-Verlag, 2005, ch. 3, pp. 63–85.
[26] C. Y.-P. Chao and S. L. Chuang, "Spin-orbit-coupling effects on the valence-band structure of strained semiconductor quantum wells," *Phys. Rev. B*, vol. 46, pp. 4110–4122, Aug 1992.
[27] J.-M. Jancu and P. Voisin, "Tetragonal and trigonal deformations in zinc-blende semiconductors: A tight-binding point of view," *Phys. Rev. B*, vol. 76, no. 11, pp. 115 202–115 204, Sep. 2007.
[28] W. G. Spitzer, F. A. Trumbore, and R. A. Logan, "Properties of heavily doped *n*-type germanium," *J. Appl. Phys.*, vol. 32, no. 10, pp. 1822–1830, 1961.
[29] J. I. Pankove and P. Aigrain, "Optical absorption of arsenic-doped degenerate germanium," *Phys. Rev.*, vol. 126, pp. 956–962, 1962.
[30] C. Haas, "Infrared absorption in heavily doped *n*-type germanium," *Phys. Rev.*, vol. 125, pp. 1965–1971, 1962.
[31] R. Newman and W. W. Tyler, "Effect of impurities on free-hole infrared absorption in *p*-type germanium," *Phys. Rev.*, vol. 105, pp. 885–886, 1957.
[32] J. Liu *et al.*, "Tensile-strained, n-type Ge as a gain medium for monolithic laser integration on Si," *Opt. Exp.*, vol. 15, no. 18, pp. 11 272–11 277, 2007.

[33] L. Carroll *et al.*, “Direct-gap gain and optical absorption in germanium correlated to the density of photoexcited carriers, doping, and strain,” *Phys. Rev. Lett.*, vol. 109, Aug. 2012, Art. ID. 057402.
[34] Y. Yamamoto, M. A. Schubert, C. Reich, and B. Tillack, “Selective lateral germanium growth for local GeOI fabrication,” *ECS J. Solid State Sci. Technol.*, vol. 3, no. 11, pp. P353–P356, 2014.
[35] J. Isenberg and W. Warta, “Free carrier absorption in heavily doped silicon layers,” *Appl. Phys. Lett.*, vol. 84, no. 13, pp. 2265–2267, Mar. 2004.